RSC Advances

PAPER

View Article Online
View Journal | View Issue

Cite this: *RSC Adv.*, 2024, **14**, 11594

Detection and photothermal inactivation of Gram-positive and Gram-negative bloodstream bacteria using photonic crystal biosensor and plasmonic core–shell

Ruth Birhanu Hayilesilassie,*[a] Abebe Belay Gemta,*[a] Fekadu Tolessa Maremi,[a] Alemayehu Getahun Kumela,[b] Kusse Gudishe[c] and Bereket Delga Dana[c]

Plasmonics and core–shell nanomaterials hold great potential to develop pharmaceuticals and medical equipment due to their eco-friendly and cost effective fabrication procedures. Despite these advancements, combating drug-resistant bacterial infections remains a global challenge. Therefore, this study aims to introduce a tailored theoretical framework for a one-dimensional (1D) photonic crystal biosensor (PCB) composed of $(ZrO_2/GaN)^N$/defect layer/$(ZrO_2/GaN)^N$, designed to detect Gram-positive and Gram-negative bloodstream bacteria employing the transfer matrix method (TMM). In addition, using the finite difference methods (FDM), the photothermal inactivation of bloodstream bacteria with plasmonic core–shell structures ($FeO@AuBiS_2$) was explored using key factors such as light absorption, heat generation, and thermal diffusion. By incorporating six dielectric layers and contaminated blood into the proposed PCB, a maximum sensitivity of 562 nm per RIU was recorded, and using rod-shaped plasmonic core–shell structures, 5.8 nm^{-1} light absorption capacity and 152 K change in temperature were achieved. The maximum detection sensitivity, light absorption, heat conduction and heat convection capacity of the proposed 1D PCB and plasmonic core–shell show an effective approach to combating drug-resistant bacteria.

Received 8th March 2024
Accepted 2nd April 2024

DOI: 10.1039/d4ra01802h

rsc.li/rsc-advances

1 Introduction

In recent years, detection and management of bloodstream infections caused by Gram-positive and Gram-negative bacteria have emerged as a critical challenge in healthcare setting.[1,2] Traditional diagnostic methods (Abbe refractometer,[3] comparing the liquid's refractive index to a known standard using a spectrometer,[4] and Snell's law[5]) often involve time-consuming culturing processes, delay detection and potentially influence patient outcomes.[6] Therefore, the advancement of modeling and experimental fabrication of photonic materials has garnered significant research attention, owing to their wide-ranging applications in imaging, drug delivery, sensing, and photothermal heat generation.[7,8] Particularly in the field of photonic sensing, two widely adopted schemes are intensity reduction (IR) and resonant wavelength shift (RWS).[9] The IR scheme revolves around measuring changes in light intensity to detect and quantify the presence of a target analyte. Which is accomplished by monitoring the reduction in the intensity of transmitted or reflected light using photodetectors or similar devices.[10] While the RWS scheme relies on measuring changes in the resonant wavelength of light to detect and quantify target analyte, that can be achieved through spectrometry or wavelength interrogation techniques.[11]

To leverage the unique light-analyte interaction and result in measurable signals, 1D, 2D, and 3D photonic crystals have been extensively studied.[12–14] In 1D photonic crystals, the periodic structure enhances the light-analyte interaction by exploiting the unique properties of their layered architecture.[15] Besides, in 2D photonic crystals, the periodic nanostructures are arranged in a 2D lattice to provide even greater control over the propagation of light, allowing for precise tuning of resonance conditions. This enables efficient coupling of light with the analyte molecules and facilitates the generation of strong and measurable biosignals.[16] Further, in the case of 3D photonic crystals, the full 3D periodicity creates a highly intricate and sophisticated light confinement environment, resulting in unique band structures and photonic bandgaps to enable tighter control over the light-analyte interaction.[17,18]

Recently, several experimental fabrication schemes and theoretical modeling frameworks were extensively investigated.

[a]*Department of Applied Physics, School of Applied Natural Sciences, Adama Science and Technology University, P.O.Box 1888, Adama, Ethiopia. E-mail: abebebelay96@gmail.com; butaabush@gmail.com*

[b]*Department of Applied Physics, College of Natural and Computational Sciences, Mekdela Amba University, P.O.Box 032, Tullu Awulia, Ethiopia*

[c]*Department of Applied Physics, College of Natural and Computational Sciences, Jinka University, Jinka, Ethiopia*

For example, Abadla *et al.*, fabricated, cost-effective, and user-friendly 1D binary PCB to measure the refractive index of milk samples changes due to fat concentration. And they reported that, the proposed sensor would be processed in a signal processing unit give an accurate estimation of the fat concentration in milk.[19] Besides, Huang *et al.*, experimentally demonstrated an adjustable lattice orientation of 2D hexagonal PCB with thin gold film coating for Epstein–Barr virus protein detection. Their work provides a method of employing the cut-off wavelength of 2D PCB to benchmark the amount of specific bindings between antigens and antibodies.[20] In addition, Kumar *et al.*, designed 2-D photonic crystal double ring resonator-based biosensor using the finite-difference time-domain (FDTD) and plane wave expansion (PWE) methods. Their study focused on detecting the Chikungunya virus in normal and infected blood cells. The results showed a transmission efficiency of 98%, a sensitivity of 3430 nm per RIU, and a low quality factor of 60.21.[21] Besides, Shojaeifar *et al.*, investigated a ternary photonic crystal with a piezo layer and piezo defect layer, demonstrating versatile tunability as a narrow band-pass filter in the THz range.[22] In addition, Razmjou *et al.*, reported a 3D photonic crystal composed of zeolitic imidazolate framework-8, with a polydopamine (PDA) coating on a silicon substrate for detecting various blood components in the wavelength range of 1.1 to 1.5 μm using FDTD method.[23] Overall, these studies illustrate that 1D photonic crystal biosensors are more efficient than their 2D and 3D counterparts due to their simple structure, simple fabrication, and integration into devices. The one-dimensional periodicity enhances the interaction between light and analytes, leading to stronger biosignals. Moreover, the straightforward design of 1D photonic crystals enables precise control over reflectance and transmittance properties, resulting in improved sensing performance and higher detection sensitivity.

In line with the need for an efficient detection mechanism, a promising approach to target bacterial inactivation is urgently required due to the development of antibiotic resistance by many bacteria.[24,25] By utilizing the advantages of various materials that possess different light-to-heat conversion mechanisms based on their electronic or bandgap structure in response to electromagnetic radiation,[26] several pioneers have revealed physical mechanisms for inactivating bacteria through heat,[27] pressure,[28] and radiation.[29] Specifically, plasmonic core–shell (PCS) structures have the potential to contribute to bacterial inactivation through optical trapping, photothermal effects, and photochemical reactions.[30] PCS-based photothermal inactivation (PTI)is a minimally invasive and drug-free treatment that uses specially engineered core–shell structures to efficiently absorb light of a specific wavelength that is highly absorbed by bacteria.[31,32] The absorbed light energy is converted into localized heat, leading to an increase in temperature at the bacterial site.[33] The temperature increase caused by the core–shell structures denatures proteins, destroys DNA, and impairs the integrity of cellular structures, ultimately resulting in bacterial inactivation or death.[34]

The efficacy of heat generation in the context of bacterial PTI is intricately tied to various factors such as the shape, size, and material composition of the core and shell of nanoparticles.[35,36] Thus, several pioneers reported the experimental and theoretical investigations of nanoparticle mediated PTI for bacterial inactivation. Annesi *et al.*, demonstrated the effective reduction of *Escherichia coli* population applying resonant laser irradiation of gold nanorods, the result shows, under near infrared illumination the temperature increase up to 50 °C in about 5 min.[37] Besides, Xie *et al.*, reported nanotip-engineered ZnO nanoarrays for photocatalytic bacteria remove, their work shows, ultrafast bactericidal rate of 97.5% for *E. coli* and 94.9% for *S. aureus* within 1 min.[38] Further, Yang *et al.*, developed a low-temperature PTT based on borneol-containing polymer-modified MXene nanosheets with the aid of near-infrared irradiation, and able to eradicate *Staphylococcus aureus* and *Escherichia coli* with more than 99.999% efficiency at ≤40 °C that is safe for the human body.[39] While, photothermal therapy shows promise, further research is needed to optimize its efficacy against different bacteria strains, determine the optimal parameters (such as core–shell design, light wavelength, intensity, and duration), and assess its safety for clinical applications.[33] The geometrical advantages of spherical, rod, and plate-shaped core–shell nanoparticles enable them to interact more effectively with incident light, leading to higher temperature heat generation compared to nanowires with similar shapes.[40] In contrast, nanowires of the same shapes may have limitations in light absorption and scattering due to their elongated structure, resulting in reduced overall heat generation efficiency.[41]

The objective of this study is to develop a theoretical framework and computational model for a 1D PCB and plasmonic core–shell system, with the goal of detecting and inactivating both Gram-positive and Gram-negative bacteria using photothermal methods. In order to assess the effect of the number of dielectric layers on the performance of the 1D PCB, the TMM was used to calculate sensitivity measurement parameters such as sensitivity, quality factor, and figure of merit. An optimal temperature was also determined for the photothermal inactivation of bloodstream bacteria to understand heat transfer dynamics and the interaction between laser light and core–shell structures.

2 Analytical model

2.1 Design analysis of photonic crystal biosensor

The main attractive optical future of photonic crystals is the ease to tune the photonic band gap (PBG) by optimizing the thickness and special characteristics of RI of each layer.[42] Hence, it allows us to hinder certain wavelength ranges from transmitting through the structure.[43] Thus, we plan a 1D PCB to be arranged as illustrated in Fig. 1. ZrO_2 is chosen for its outstanding optical properties, including transparency to visible light, excellent optical clarity, relatively low thermal conductivity, and thermal stability.[44] These qualities make it ideal for use in high-temperature environments without compromising its optical performance.[19] In addition, GaN has been chosen for its unique optical properties (including a wide bandgap, allowing efficient operation in the ultraviolet and visible light spectrum; a high refractive index, enabling effective light confinement and manipulation crucial for enhancing biosensor sensitivity and selectivity; low optical losses essential for maintaining a high

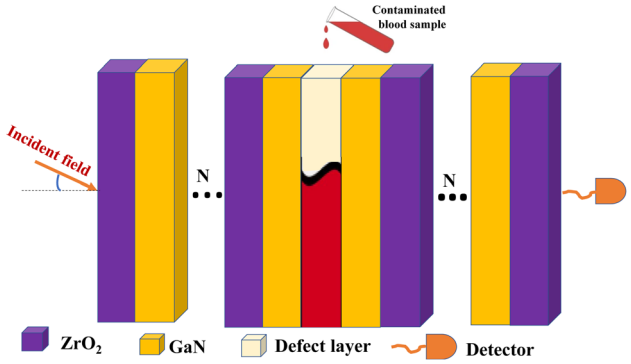

Fig. 1 Schematic diagrams of the propsed one-dimensional photonic crystal biosensor.

signal-to-noise ratio; and chemical stability and resistance to corrosion, making it suitable for long-term and reliable operation in biological sensing environments),[45,46] making it an ideal dielectric layer for PCB. Hence, as the constituents are arranged in a multi-layer structure, the TMM was used to model light interaction with the materials in the structure.

Following, employing TMM the optical parameters such as refractive index, thickness of layers, and absorption coefficients are used to calculate the transmission and reflection of light through multi-layer structures. Therefore, the refractive index of each photonic crystal constituents are dispensed in eqn (1) and (2) as,[19,45]

$$n_{ZrO_2}{}^2(\lambda) = 1 + \frac{1.347091\lambda^2}{\lambda^2 - 0.00391162685} + \frac{2.117788\lambda^2}{\lambda^2 - 0.02780189412} + \frac{9.452943\lambda^2}{\lambda^2 = 591.490125}, \quad (1)$$

and

$$n_{GaN}{}^2(\lambda) = 3.60 + \frac{1.75\lambda^2}{\lambda^2 - 0.256^2} + \frac{4.1\lambda^2}{\lambda^2 - 17.86^2}. \quad (2)$$

Furthermore, Gram-positive bacteria possess a robust peptidoglycan cell wall that retains the crystal violet stain during the gram staining process,[47] while Gram-negative bacteria feature a thinner peptidoglycan layer surrounded by an outer membrane containing lipopolysaccharides.[48] This difference in cell wall composition contributes to Gram-negative bacteria having a higher refractive index compared to Gram-positive bacteria.[49] This structural variation plays a significant role in determining their response to antibiotics, susceptibility to disinfectants, and overall pathogenicity.[47,48] The refractive index values of the bacteria used in this study are presented in Table 1.

The RI variation due to concentration type and level variation of contaminated human blood cell takes the form,[56]

$$n_{CB} = n_{NB} + RI_s cons. \quad (3)$$

where, n_{CB} is RI of contaminated blood, n_{NB} is RI of normal blood cell and RI_s is specific refractive index of sample, and cons. is concentration level.

Table 1 RI of Gram positive and Gram negative pathogenic bacteria

Bacteria type	Bacteria name	RI	Ref.
Gram positive	*Staphylococcus aureus*	1.416	50
	Bacillus anthracis	1.383	51
	Streptococcus haemolyticus	1.410	52
Gram negative	*Escherichia coli*	1.585	53
	Pseudomonas aeruginosa	1.371	54
	Serratia marcescens	1.556	55

To this end, the interaction of incident light field with proposed photonic crystal can be expressed by TMM using,[19]

$$F = \begin{pmatrix} F_{11} & F_{12} \\ F_{21} & F_{22} \end{pmatrix}, = (f_1 f_2)^N f_3 (f_1 f_2)^N, \quad (4)$$

where, F_{11}, F_{12}, F_{21}, and F_{22} are elements of total matrix, N is number of dielectric layer, and f_i for $i = 1, 2, 3$ represents characteristics transfer matrix each given by,

$$f_i = \begin{bmatrix} \cos\alpha_j & \frac{i\sin\alpha_j}{j} \\ i\beta_j \sin\alpha_j & \cos\alpha_j \end{bmatrix}. \quad (5)$$

Here, $\alpha_j = \left(\frac{2\pi}{\lambda}\right) n_j d_{j\cos\theta_j}$, $\beta_j = n_j\sqrt{\varepsilon_0\mu_0}$, and $\theta_j = \sin^{-1}\left(\frac{\sin\theta_0}{n_j}\right)$ in which λ is pumping wavelength, d_j is thickness of each layer, ε_0 is permittivity of free space, μ_0 is permeability of free space, and θ_0 is angle of incidence for transverse electric (TE) mode.

Following this, the reflectivity (R) in-terms of reflection coefficient (r) takes the from,[57]

$$r = \frac{F_{21}}{F_{11}}, \rightarrow R = |r|^2. \quad (6)$$

Employing eqn (6) the reflectivity *versus* wavelength will plotted to dispensed the sensors performance of proposed biosensor in-terms of sensitivity $\left(S = \frac{\Delta\lambda_{res}}{\Delta n}\right)$,[19] quality factor (QF = $\Delta\lambda_{res}$/FWHM), $\left(QF = \frac{\lambda_{res}}{FWHM}\right)$ figure of merit [45] and resolution limit $\left(RL = \frac{2FWHM}{3(S)^{0.25}}\right)$[58] will dispensed in Section 3.

In addition to the theoretical analysis, the authors recommend following experimental procedures for practical fabrication of the proposed biosensor: start by preparing cost-effective zirconium and oxygen precursors, such as zirconium alkoxides or salts.[59] Then, create a sol by dissolving the zirconium precursor in a solvent like ethanol to obtain a uniform solution, adding water for hydrolysis and polycondensation, ensuring proper mixing while controlling pH. Next, let the gel age to solidify, forming a structured network. By optimizing parameters like precursor concentration and solvent choice, the sol–gel method can efficiently synthesize ZrO_2 for photonic crystal applications.[60] For GaN substrate synthesis, consider hydride vapor phase epitaxy (HVPE) for fast growth rates and follow with ammonothermal growth for high-quality GaN crystals.[61] In addition, in preparing defect layer some physical properties like

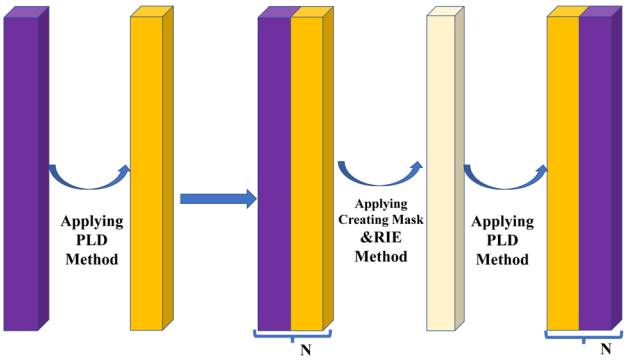

Fig. 2 Schematic diagram of each steps for experimental fabrication of proposed one-dimensional photonic crystal biosensor.

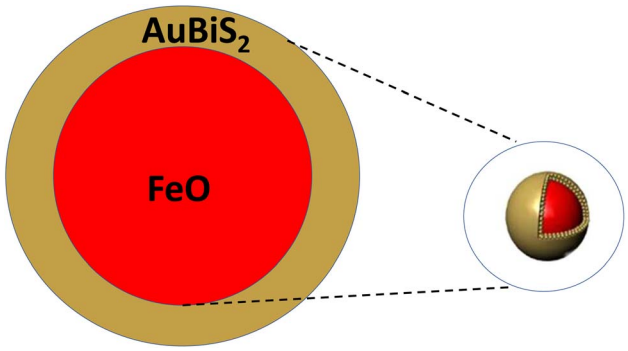

Fig. 3 Schematic diagrams of the proposed core–shell structures.

biocompatiblty, and functional groups that optimize biomolecular binding affinity are must be considered.

Following the substrate preparation, the assembly of the proposed PCB follows a set of recommended procedures. Firstly, GaN film is ablated onto a ZrO_2 substrate using pulsed laser deposition under controlled conditions to ensure uniformity and minimal defects. This technique is repeated based on the number of dielectric layers (N) utilized. Pulsed laser deposition (PLD) is chosen for its precision and control in producing high-quality thin films. Next, to deposit a defect layer onto the GaN substrate, start by creating a mask on the GaN surface using lithography to outline areas for defect formation. Then, use reactive ion etching (RIE) to selectively remove GaN material in the masked regions, inducing controlled defects. And deposit dielectric substrate onto defect layer following the above techniques. Finally, confirm the formation of the defect layer through SEM imaging and electrical characterization to guarantee improved biosensor sensitivity and performance. The overall assembly procedure is outlined in Fig. 2.

2.2 Theoretical model of plasmonic core–shell heat generation

The theoretical model of the photothermal response of core–shell structures involves understanding the underlying physical processes and developing mathematical equations to describe the heat generation and transfer mechanisms.[62,63] This helps in predicting and optimizing the behavior of core–shell structures under different light sources, material properties, and geometries.[64] Therefore, in this work we proposed spherical, rod, and plate shaped FeO@$AuBiS_2$ core–shell that arranged as shown in Fig. 3. In selecting shape we consider: spherical geometry ensures light absorption from all directions, enabling effective light absorption and conversion into heat.[65] Rod-shaped core–shell nanoparticles offer adjustable aspect ratios that enhance interaction with incident light, promoting efficient heat conversion.[66] Plate-shaped core–shell nanoparticles provide a large surface area, facilitating improved light absorption and enhancing their capacity for heat generation.[67]

In addition, in selecting shell ($AuBiS_2$), the exceptional plasmonic property, production of reactive oxygen species, photothermal conversion efficiency, and excellent chemical properties are considered.[68] In addition, FeO is selected for its high photon absorption that used to cool the overheated cell.[69]

The first step to express light-to-heat conversion process is calculated employing absorption cross-sections (C_{abs}), extinction coefficients (C_{ext}), and light absorption capacity (A_{abs}),[70] using well known Mie theory is given by eqn (7) to (9),[71,72]

$$C_{ext} = \frac{2\pi}{k_j}\sum_{j=1}^{\infty}(2j+1)\mathrm{Re}(a_j + b_j), \tag{7}$$

$$C_{sca} = \frac{2\pi}{k_j}\sum_{j=1}^{\infty}(2j+1)\mathrm{Re}\left(|a_j|^2 + |b_j|^2\right), \tag{8}$$

and

$$C_{abs} = C_{ext} - C_{sca}. \tag{9}$$

In which the light absorption capacity is $A_{abs} = \frac{C_{abs}}{V_p}$, for volume of nanosphere ($V_p = 4/3\pi r_j^3$), volume of nanorod ($V_p = \pi r_j^2 l$ here l is length of rod), and volume of plate ($V_p = \pi r_j^2 t$ t is thickness of plate core–shell). Where,

$$a_j = -\frac{X_j^{TM}}{X_j^{TM} + iY_j^{TM}}, b_j = -\frac{X_j^{TE}}{X_j^{TE} + iY_j^{TE}}. \tag{10}$$

For which

$$X_j^{TE} = \begin{vmatrix} \eta_j(k_c r_c) & \eta_j(k_s r_c) & \xi_j(k_s r_c) & 0 \\ \frac{\psi_j'(k_c r_c)}{\mu_c} & \frac{\psi_j'(k_s r_c)}{\mu_s} & \frac{\psi_j'(k_s r_c)}{\mu_s} & 0 \\ 0 & \eta_j(k_s r_s) & \xi_j(k_s r_s) & \eta_j(k_s r_s) \\ 0 & \frac{\psi_j'(k_s r_s)}{\mu_c} & \frac{\Phi_j'(k_s r_s)}{\mu_s} & \frac{\psi_j'(k_s r_s)}{\mu_m} \end{vmatrix}, \tag{11}$$

and

$$Y_j^{TE} = \begin{vmatrix} \eta_j(k_c r_c) & \eta_j(k_s r_c) & \xi_j(k_s r_c) & 0 \\ \frac{\psi_j'(k_c r_c)}{\mu_c} & \frac{\psi_j'(k_s r_c)}{\mu_s} & \frac{\psi_j'(k_s r_c)}{\mu_s} & 0 \\ 0 & \eta_j(k_s r_s) & \xi_j(k_s r_s) & \eta_j(k_s r_s) \\ 0 & \frac{\psi_j'(k_s r_s)}{\mu_c} & \frac{\Phi_j'(k_s r_s)}{\mu_s} & \frac{\Phi_j'(k_s r_s)}{\mu_m} \end{vmatrix}. \tag{12}$$

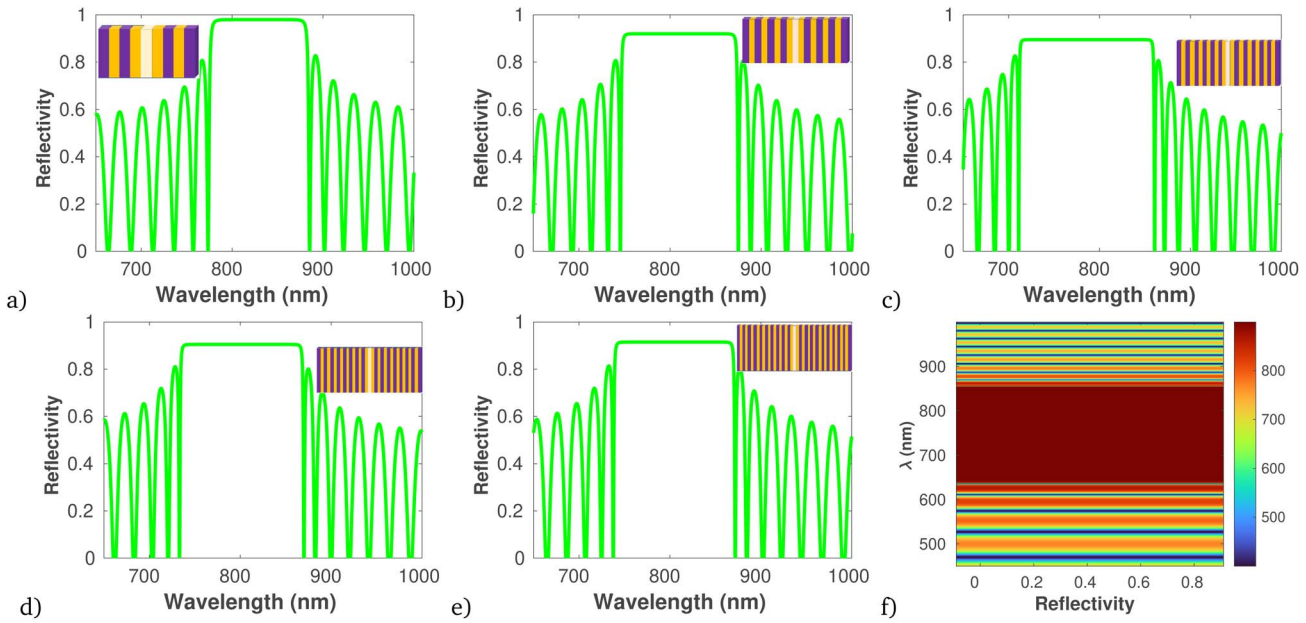

Fig. 4 Plot of photonic band structure of different number of dielectric layer *versus* wavelength at $T = 20$ °C, and angle of incidence 60°. (a) $N = 2$, (b) $N = 4$, (c) $N = 6$, (d) $N = 8$, (e) $N = 10$, and (f) electric field profile for $N = 6$, plotted using Matlab2023b.

Here, r_c and r_s are inner and outer radius of core–shell respectively, X_j and Y_j are determinants, η_j is spherical Bessl function, ξ_j is spherical Nuemann function, ψ_j and Φ_j are Riccati–Bessel function, and $k_j = \frac{2\pi}{\sqrt{\varepsilon_j}\lambda}$ is wave number for ε_j is permittivity in which j = c,s,m.

Once the light is absorbed by the core–shell structure, it is converted into heat through various mechanisms, such as electron-phonon relaxation, nonradiative transitions, and phonon–phonon interactions.[73] The absorbed energy is transformed into heat, causing increase in temperature that expressed by conversion efficiency.[74] $\delta = \frac{Cm\Delta T}{PA\tau}$ Here, C is specific heat, m is mass of proposed core–shell, P is power density of incident light, A is radiation area, and τ is radiation time. The main focus of this work is inactivation of bloodstream bacteria in blood sample, so the heat flow of from core–shell

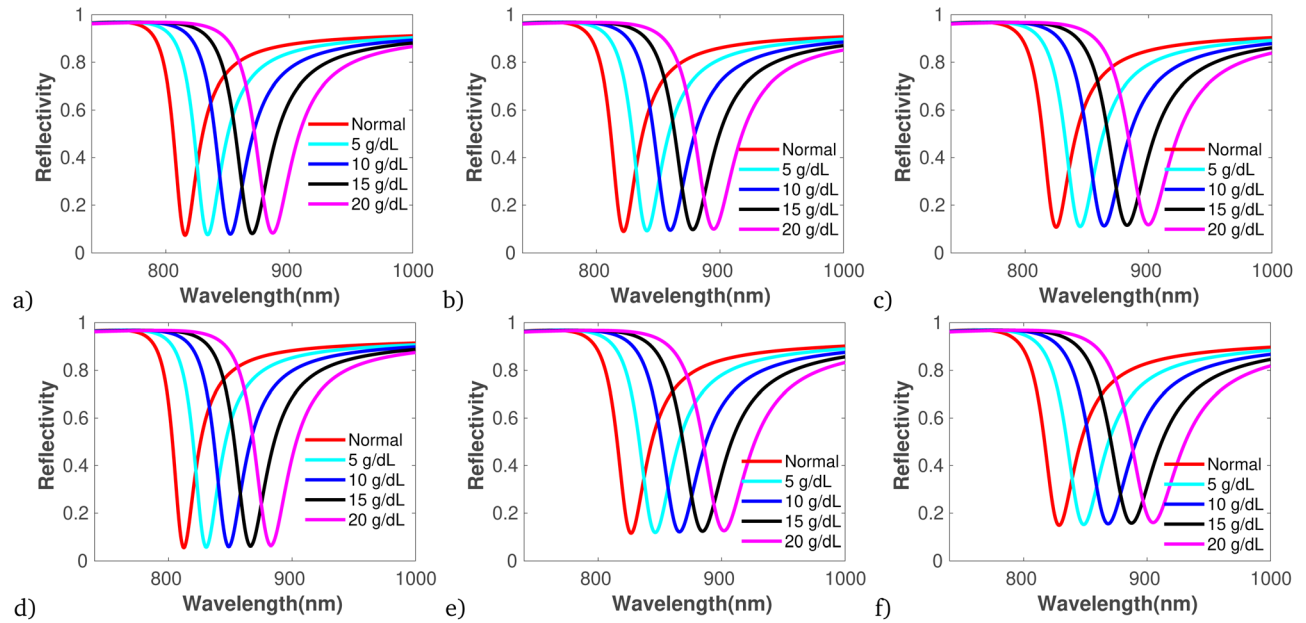

Fig. 5 Plot of reflectivity *versus* wavelength under band edge modes for different concentration of bacteria contaminated blood, using data presented in Table.1, at $T = 20$ °C, and angle of incidence 60°. (a) *Bacillus anthracis*, (b) *Streptococcus haemolyticus*, (c) *Staphylococcus aureus*, (d) *Pseudomonas aeruginosa*, (e) *Serratia marcescens*, (f) *Escherichia coli*.

Table 2 Performance analysis of different number of dielectric layer using data presented Fig. 4 in line with sensitivity performance measurement parameters

Number of layer	$\Delta\lambda_{res}$ (nm)	Δn	FWHM	S (nm per RIU)	FoM	QF (RIU^{-1})	RL
2	—	—	35	—	—	—	—
4	20	0.1	57.5	200	3.47	0.347	144.16
6	15	0.025	75	600	8	0.20	247.46
8	13	0.03	78	433.3	5.56	0.170	237.20
10	12	0.038	81	316	3.90	0.148	227.68

Table 3 Sensitivity performance analysis of different bloodstream bacteria with different concentration using data presented Fig. 5. Where, BS is bacterial specification, GP is Gram-positive, GN is Gram negative, BN is bacteria name, BA is *Bacillus anthracis*, SH is *Streptococcus haemolyticus*, SA is *Staphylococcus aureus*, PA is *Pseudomonas aeruginosa*, SM is *Serratia marcescens*, and EC is *Escherichia coli*

BS	BN	Cons.	$\Delta\lambda_{res}$ (nm)	Δn	FWHM	S (nm per RIU)	FoM	QF (RIU^{-1})	RL
GP	BA	5	0.47	0.0025	2.02	188	0.232	93.06	0.363
		10	0.3	0.0014	2.19	214.28	0.136	97.84	0.381
		15	0.28	0.0010	2.53	280	0.110	110.67	0.412
		20	0.17	0.00032	2.71	531.25	0.062	196.03	0.376
	SH	5	0.50	0.002	2.8	250	0.178	89.28	0.469
		10	0.45	0.0017	3.1	264.70	0.145	85.38	0.512
		15	0.42	0.001	3.33	276.31	0.126	82.97	0.544
		20	0.37	0.00089	3.69	415.73	0.100	112.66	0.545
	SA	5	0.52	0.0021	3.17	247.61	0.164	78.11	0.532
		10	0.48	0.0018	3.42	266.67	0.140	77.97	0.564
		15	0.43	0.0015	4.06	286.67	0.105	7.60	0.651
		20	0.41	0.0010	4.08	410	0.100	100.49	0.604
GN	PA	5	0.51	0.003	2.1	170	0.124	80.95	0.387
		10	0.50	0.0028	2.40	178.5	0.208	74.37	0.437
		15	0.48	0.0021	2.58	228.57	0.186	88.59	0.442
		20	0.46	0.0011	2.95	418.18	0.155	141.75	0.434
	SM	5	0.53	0.0028	3.28	189.28	0.161	57.70	0.589
		10	0.51	0.0025	3.57	204	0.142	57.14	0.629
		15	0.48	0.0016	3.97	300	0.120	68.18	0.635
		20	0.47	0.0010	4.4	470	0.106	106.81	0.630
	EC	5	0.55	0.0032	3.67	171.87	0.149	46.83	0.675
		10	0.53	0.0028	3.88	189.28	0.136	48.78	0.697
		15	0.51	0.0021	3.90	242.85	0.130	62.26	0.658
		20	0.50	0.00089	4.51	561.79	0.110	124.56	0.617

(light absorber) to the sample (contaminated blood sample) is given by conduction energy $\left(H_{cond} = \frac{A}{L}(T_{cs} - T_{sam})\right)$, where, ξ is thermal conductivity, L is conduction length, and T_{cs} and T_{sam} are temperature raised by core–shell and temperature of sample respectively. Hence the proposed sample is fluid, the heat energy transfer induced by movement of fluid is given by convection energy ($H_{conv} = C_h A(T_{cs} - T_{sam})$, for C_h is heat transfer coefficient). Further, by applying quasi static electromagnetic field equation, the relation between change in

Table 4 Performance analysis of various PCB reported in recent years. Where, PWE is plane wave expansion, FDTD is finite difference time domain, CCW is coupled cavity waveguide

Sample	PCB arrangement	Method	S (nm per RIU)	QF (RIU^{-1})	FoM	Ref.
Glucose	2D	PWE and FDTD	795	53.5	33.07	82
Glucose	1D ternary	TMM	768.3	1239.3	394.017	83
Blood	1D binary	TMM	71.25	20.96	—	84
Blood	1D binary	TMM	203.09	1569	0.0093	85
Blood	2D	FDTD	217.5	—	817.66	86
Biotargets	CCW	PWE and FDTD	203	—	13 360	87
Blood	1D binary	TMM	562	124.6	0.110	This work

temperature (ΔT) and absorption coefficient resulted from chemical and physical characteristics of sample, core–shell and pumping laser takes the form,[75]

$$\Delta T = \left(\frac{C_{\text{abs}}}{C_{\text{sam}} V_{\text{cs}} \rho_{\text{cs}}}\right)\phi. \quad (13)$$

where, C_{sam} is specific heat capacity of sample, V_{cs} is volume of core–shell, ρ_{cs} is density of core–shell, and ϕ is the optical flux of incident light.

To experimentally fabricate FeO@AuBiS$_2$ core–shell structures, begin by synthesizing FeO nanoparticles through a method such as co-precipitation or thermal decomposition.[76] Next, prepare the AuBiS$_2$ shell by adding gold and bismuth precursors to a sulfur-containing solution under controlled conditions to facilitate shell formation around the FeO nanoparticles.[68] Utilize techniques like solvothermal or sonochemical methods for the core–shell assembly, ensuring proper shell growth and uniform coverage.[77] Characterize the FeO@AuBiS$_2$

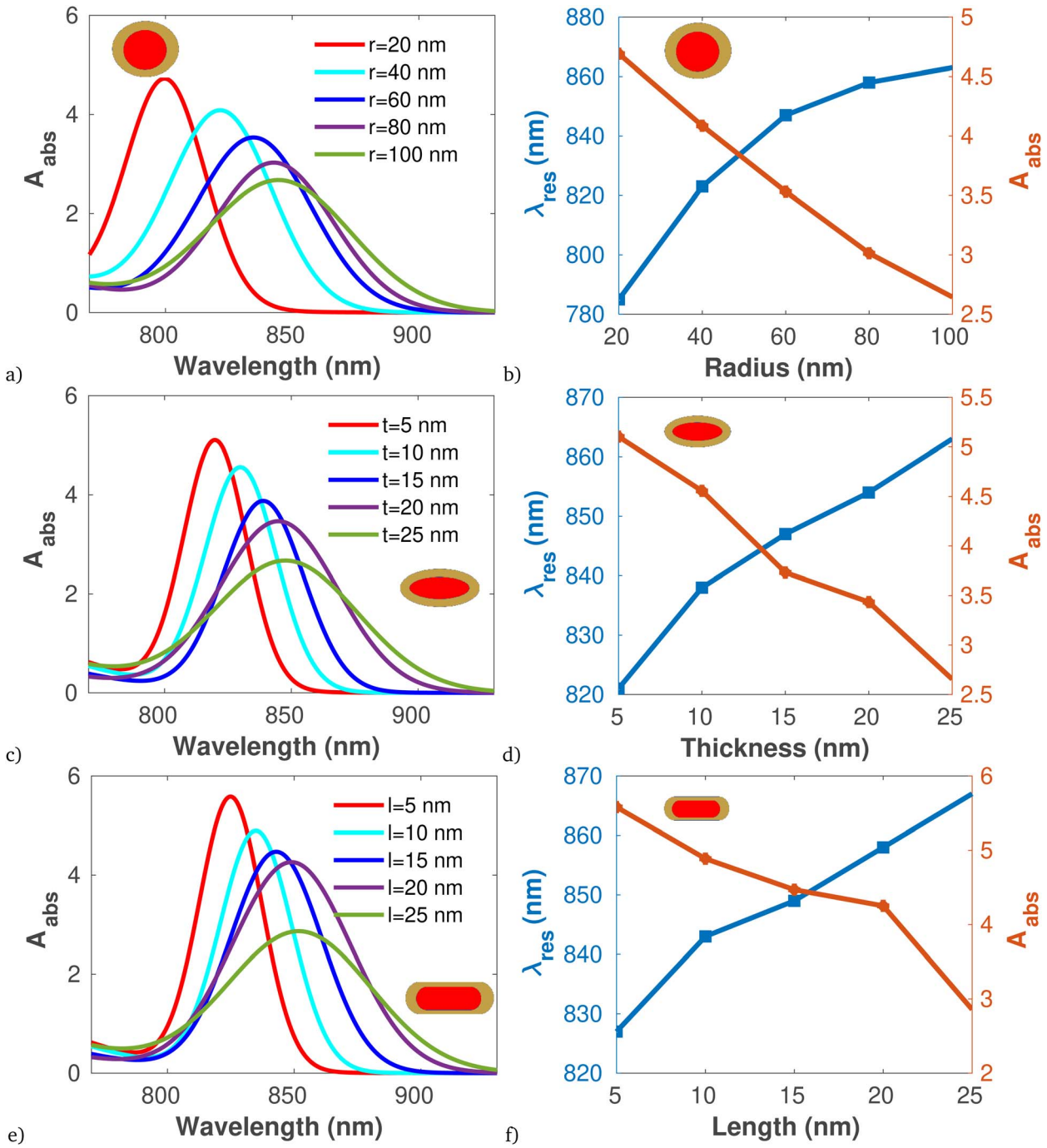

Fig. 6 Plot of Absorption cross section and resonant peak *versus* wavelength and thickness for different shape of core–shell using data presented in Table 1, at 808 nm pumping wave length. (a)and (b) Spherical core–shell. (c and d) Plate shaped core–shell. (e and f) Rod shaped core–shell.

core–shell structures using analytical techniques like transmission electron microscopy (TEM) and X-ray diffraction (XRD) to confirm the presence of the core and shell components.[78] Adjust synthesis parameters such as precursor concentrations and reaction times to optimize the core–shell structure for potential photothermal applications.

3 Result and discussions

The numerical analysis procedures for optimizing the sensitivity of the proposed 1D PCB structure for detecting bloodstream bacteria were detailed in eqn (1)–(6). Using Matlab2023b, we characterized the spectral response by varying the number of dielectric layers (refer to Fig. 4) and adjusting the concentration of bacterial-infected blood (refer to Fig. 5). (Fig. 4a–c) clearly demonstrate that with an increase in the number of dielectric layers, the PBG of the proposed structure expands due to each additional layer introduces new opportunities for light waves to be filtered out based on their frequencies, resulting in a broader PBG that covers a wider range of wavelengths. However, beyond the optimal number of layers ($N = 6$), the PBG diminishes (as shown in Fig. 4d and e) as a fact that as the number of dielectric layers 1D PCB increased beyond the optimal point, the constructive interference that initially contributed to the formation of the PBG can experience interference patterns that lead to destructive interference, this agree with recently reported literature.[79,80] In addition, (Fig. 4f) illustrates the electric field profile within the photonic crystal structure at the optimal number of dielectric layers.

Further, using the data provided in (Fig. 4a–e), Table 2 illustrates the comprehensive performance analysis of each number of dielectric layers. The result reveals that as the PBG increases, there is a corresponding increase in S, FoM, QF, and RL.

Moreover, Fig. 5 displays the reflectivity *versus* wavelength for bacterial-contaminated blood samples, specifically GP (Fig. 5a–c) and GN (Fig. 5c–f), with varying concentrations and specifications while keeping the number of dielectric layers fixed to optimal sensitivity under band edge modes.[81] The figures clearly demonstrate that as the sample concentration increases, the reflectivity spectra broaden and shift towards longer wavelengths, leading to a broader FWHM. Hence, the sample concentration increases can be attributed to the increased refractive index contrast, changes in the effective optical path length, and the influence of surface plasmon resonance effects induced by the binding of analyte molecules. These effects collectively alter the spectral response of the photonic crystal biosensor, providing valuable information about the concentration and interaction of biomolecules with the sensor surface. Additionally, the sensitivity variations at each sample concentration are illustrated in Table 3. Thus Table 3 reveal the maximum S of 562 nm per RIU, FoM of 0.232, QF of 196.03/RIU, and RL of 0.697 that outperform recently reported work of.[19]

Finally, we have performed a comparative analysis of our result with recent studies conducted between 2021 and 2024. The data gathered from this study has been collated and is summarized in Table 4. The outcomes underscore the potential of the proposed structure for integration into the development of exceptionally sensitive biophotonic sensors.

Table 5 Heat conversion analysis of different shape plasmonic core–shell using $C_{cs} = 1.2$ kJ kg^{-1}, $C_{sam} = 4.18$ kJ kg^{-1}, $C_h = 10.145$, $m_{cs} = 2.22$ kg s^{-1}, $m_{sam} = 2.0.8$ kg s^{-1}, and $\phi = 808$ nm parameters from literature[91–93]

Core–shell shape	Parameters	H_{con}	H_{conv}	ΔT
Sphere	$r = 10$ nm	65.831	0.543	95.46
	$r = 15$ nm	57.71	0.817	125.53
	$r = 20$ nm	51.214	1.087	148.52
	$r = 25$ nm	45.89	1.360	166.37
Plate	$t = 5$ nm, $r = 10$ nm	66.43	0.522	96.32
	$t = 10$ nm, $r = 15$ nm	58.44	0.783	127.10
	$t = 15$ nm, $r = 20$ nm	52.01	1.044	158.83
	$t = 20$ nm, $r = 25$ nm	46.73	1.305	169.420
Rod	$l = 5$ nm, $r = 10$ nm	66.76	0.509	96.81
	$l = 10$ nm, $r = 15$ nm	58.85	0.764	128
	$l = 15$ nm, $r = 20$ nm	52.46	1.02	152.16
	$l = 20$ nm, $r = 25$ nm	47.21	1.27	171.16

On the other hand, the photothermal response of the proposed core–shell structure is illustrated in Fig. 6 using eqn (8). It is evident that as the radius, thickness, and length of the core–shell increase, the absorption cross-section also increases. Comparing (Fig. 6a–f), it is apparent that core–shell structures in rod shapes exhibit the highest light absorption capacity of 5.8 nm^{-1}. Subsequently, the heat conversion analysis of the proposed core–shell is presented in Table 5. The data clearly indicates that an increase in the size of the core–shell results in a greater temperature difference within the sample, attributed to the increased distance for heat transfer. This leads to a reduction in the rates of heat conduction and convection as the larger core–shell size diminishes the efficiency of heat transfer across the structure. Moreover, comparing the heat generated by proposed core–shell with other modalities of heat based bacteria inactivation, it is evident that the proposed work can effectively used to inactivate both Gram-positive and Gram-negative bacteria.[88–90]

4 Conclusion

In summary, to evaluate the sensing performance of the proposed biosensor, we initially conducted a numerical analysis of reflection spectra with varying dielectric layers and concentrations of bacterial-contaminated blood using TMM. The simulation results revealed a maximum sensitivity of 600 nm per RIU for $N = 6$. Additionally, for $N = 6$ when incorporating bacterial-infected blood samples into defect layers, a sensitivity of 562 nm per RIU was achieved. Furthermore, utilizing Mie theory, we explored the heat generation capabilities of core–shell structures by adjusting their shape, diameter, thickness, and length. The findings indicated that rod-shaped core–shells produced temperature changes ranging from 40 °C to 80 °C, demonstrating effectiveness in deactivating both Gram-positive and Gram-negative bacteria.

Data availability

Data underlying the results presented in this paper are not publicly available at this time but may be obtained from the authors upon reasonable request.

Conflicts of interest

The authors declare that they have no known competing financial interests or personal relationships that could have appeared to influence the work reported in this paper.

Acknowledgements

The first author thanks Mekdela Amba University for partial sponser this work.

References

1 D. Giacobbe, T. Giani, M. Bassetti, A. Marchese, C. Viscoli and G. Rossolini, *Clin. Microbiol. Infect.*, 2020, **26**, 713–722.
2 R. Birhanu, A. B. Gemta, F. Tolessa Maremi and A. G. Kumela, *J. Opt.*, 2024, 1–12.
3 I. Y. Yanina, A. P. Popov, A. V. Bykov, I. V. Meglinski and V. V. Tuchin, *J. Biomed. Opt.*, 2018, **23**, 016003.
4 S. Kedenburg, M. Vieweg, T. Gissibl and H. Giessen, *Opt. Mater. Express*, 2012, **2**, 1588–1611.
5 A. V. Shukla, Clinical optics primer for ophthalmic medical personnel: a guide to laws, *Formulae, Calculations, and Clinical Applications*, Slack Incorporated, 2009.
6 M. Pradella, R. M. Dorizzi, F. Rigolin and B. E. Statland, *Crit. Rev. Clin. Lab. Sci.*, 1988, **26**, 195–242.
7 M. T. Sohail, M. Wang, M. Shareef and P. Yan, *Infrared Phys. Technol.*, 2024, 105127.
8 Z. Zhang, H. Zhu, W. Zhang, Z. Zhang, J. Lu, K. Xu, Y. Liu and V. Saetang, *Carbon*, 2023, 118356.
9 M. Al Mahfuz, M. A. Hossain, E. Haque, N. H. Hai, Y. Namihira and F. Ahmed, *IEEE Sens. J.*, 2020, **20**, 7692–7700.
10 A. Ahmadivand and B. Gerislioglu, *Laser Photonics Rev.*, 2022, **16**, 2100328.
11 A. A. Rifat, G. A. Mahdiraji, Y. Shee, M. J. Shawon and F. M. Adikan, *Procedia Eng.*, 2016, **140**, 1–7.
12 G. M. Paterno, L. Moscardi, S. Donini, D. Ariodanti, I. Kriegel, M. Zani, E. Parisini, F. Scotognella and G. Lanzani, *J. Phys. Chem. Lett.*, 2019, **10**, 4980–4986.
13 Y.-L. Ji, L.-X. Gao and Y. Tian, *Mater. Adv.*, 2023, **4**, 542–550.
14 Y. Xu, P. Bai, X. Zhou, Y. Akimov, C. E. Png, L.-K. Ang, W. Knoll and L. Wu, *Adv. Opt. Mater.*, 2019, **7**, 1801433.
15 A. Getahun, A. B. Gemta, A. Kebede, R. Birhanu, H. D. Mekonnen, U. Sherefedin and K. Woldegiorges, *Nanoscale Adv.*, 2023, **5**, 6382–6399.
16 T. Lu, W. Peng, S. Zhu and D. Zhang, *Nanotechnology*, 2016, **27**, 122001.
17 S. Feng, J.-H. Jiang, A. Al Rashid and S. John, *Opt. Express*, 2016, **24**, 12166–12191.
18 J. Li and K. Nallappan, *Opt. Mater. Express*, 2019, **9**, 1640–1653.
19 K. M. Abohassan, H. S. Ashour and M. M. Abadla, *RSC Adv.*, 2021, **11**, 12058–12065.
20 Y.-T. Chen, Y.-Y. Liao, C.-C. Chen, H.-H. Hsiao and J.-J. Huang, *Sens. Actuators, B*, 2019, **291**, 81–88.
21 S. Sharma, A. Kumar, K. S. Singh and H. K. Tyagi, *Optik*, 2021, **237**, 166575.
22 A. S. Firouzjaei, D. Kalhor, M. Shojaeifar and H. Goudarzi, *Optik*, 2023, **288**, 171248.
23 M. Nankali, Z. Einalou, M. Asadnia and A. Razmjou, *ACS Appl. Bio Mater.*, 2021, **4**, 1958–1968.
24 T. Yu, G. Jiang, R. Gao, G. Chen, Y. Ren, J. Liu, H. C. van der Mei and H. J. Busscher, *Expert Opin. Drug Delivery*, 2020, **17**, 1151–1164.
25 A. S. Ezeuko, M. O. Ojemaye, O. O. Okoh and A. I. Okoh, *J. Water Proc. Eng.*, 2021, **41**, 102041.
26 J. U. Kim, S. Lee, S. J. Kang and T.-i. Kim, *Nanoscale*, 2018, **10**, 21555–21574.
27 R. Lv, D. Liu and J. Zhou, *Curr. Opin. Food Sci.*, 2021, **42**, 31–36.
28 R. Sehrawat, B. P. Kaur, P. K. Nema, S. Tewari and L. Kumar, *Food Sci. Biotechnol.*, 2021, **30**, 19–35.
29 P. Shaw, N. Kumar, S. Mumtaz, J. S. Lim, J. H. Jang, D. Kim, B. D. Sahu, A. Bogaerts and E. H. Choi, *Sci. Rep.*, 2021, **11**, 14003.
30 Y. Zhang, H. Yan, J. Tang, P. Li, R. Su, H. Zhong and W. Su, *J. Photochem. Photobiol., A*, 2022, **425**, 113722.
31 A. Gharatape, S. Davaran, R. Salehi and H. Hamishehkar, *RSC Adv.*, 2016, **6**, 111482–111516.
32 S. Mondal, J. L. Montaño-Priede, S. Park, J. Choi, V. H. M. Doan, T. M. T. Vo, T. H. Vo, N. Large, C.-S. Kim, J. Oh, *et al.*, *J. Adv. Res.*, 2022, **41**, 23–38.
33 G. Guan, K. Y. Win, X. Yao, W. Yang and M.-Y. Han, *Adv. Healthcare Mater.*, 2021, **10**, 2001158.
34 D. Hu, L. Zou, B. Li, M. Hu, W. Ye and J. Ji, *ACS Biomater. Sci. Eng.*, 2019, **5**, 5169–5179.
35 H. Liu, F. Xing, Y. Zhou, P. Yu, J. Xu, R. Luo, Z. Xiang, P. M. Rommens, M. Liu and U. Ritz, *Mater. Des.*, 2023, 112231.
36 X. Qi, Y. Xiang, E. Cai, X. Ge, X. Chen, W. Zhang, Z. Li and J. Shen, *Coord. Chem. Rev.*, 2023, **496**, 215426.
37 F. Annesi, A. Pane, M. A. Losso, A. Guglielmelli, F. Lucente, F. Petronella, T. Placido, R. Comparelli, M. G. Guzzo, M. L. Curri, *et al.*, *Materials*, 2019, **12**, 1530.
38 Y. Xie, X. Qu, J. Li, D. Li, W. Wei, D. Hui, Q. Zhang, F. Meng, H. Yin, X. Xu, *et al.*, *Sci. Total Environ.*, 2020, **738**, 139714.
39 N. J. Yang and I. M. Chiu, *J. Mol. Biol.*, 2017, **429**, 587–605.
40 J. Boken, P. Khurana, S. Thatai, D. Kumar and S. Prasad, *Appl. Spectrosc. Rev.*, 2017, **52**, 774–820.
41 V. Kudryavtseva and G. B. Sukhorukov, *Adv. Mater.*, 2024, 2307675.
42 R. K. Gangwar, A. K. Pathak and S. Kumar, *Photonics*, 2023, 1199.
43 K. Zhu, C. Fang, M. Pu, J. Song, D. Wang and X. Zhou, *J. Mater. Sci. Technol.*, 2023, **141**, 78–99.

44 S. Bhaskar, E. W. Awin, K. H. Kumar, A. Lale, S. Bernard and R. Kumar, *Sci. Rep.*, 2020, **10**, 430.
45 A. H. Aly, B. Mohamed, S. Awasthi, S. A. O. Abdallah and A. Amin, *Sci. Rep.*, 2023, **13**, 9422.
46 Y.-n. Zhang, Y. Zhao and R.-q. Lv, *Sens. Actuators, A*, 2015, **233**, 374–389.
47 M. J. Wilhelm, J. B. Sheffield, M. Sharifian Gh, Y. Wu, C. Spahr, G. Gonella, B. Xu and H.-L. Dai, *ACS Chem. Biol.*, 2015, **10**, 1711–1717.
48 N. Paracini, E. Schneck, A. Imberty and S. Micciulla, *Adv. Colloid Interface Sci.*, 2022, **301**, 102603.
49 J. Bai, E. Yang, P.-S. Chang and S. Ryu, *Enzyme Microb. Technol.*, 2019, **128**, 40–48.
50 S. Gandhi and S. K. Awasthi, *Mater. Today: Proc.*, 2023, **29**, 101428.
51 S. Pandiaraj, M. Muthuramamoorthy, N. Alanazi and A. N. Alodhayb, *Plasmonics*, 2024, 1–9.
52 A. H. Aly, S. Awasthi, M. Mohaseb, Z. Matar and A. Amin, *Crystals*, 2022, **12**, 220.
53 W. P. Van De Merwe, J. Czégé, M. E. Milham and B. V. Bronk, *Appl. Opt.*, 2004, **43**, 5295–5302.
54 Y. P. Liu, PhD thesis, Université Paris-Est, 2016.
55 G. Rong, Y. Zhang, Y. Chen, J. Chen, N. Jiang and J. C. Merchuk, *Cytometry, Part A*, 2022, **101**, 254–263.
56 M. H. Sani and S. Khosroabadi, *IEEE Sens. J.*, 2020, **20**, 7161–7168.
57 A. G. Kumela, A. B. Gemta, A. K. Hordofa, T. A. Desta, M. Dangish and H. D. Mekonnen, *Sens. Int.*, 2023, **4**, 100232.
58 A. G. Kumela, A. B. Gemta, A. K. Hordofa, H. Dagnaw, U. Sheferedin and M. Tadesse, *AIP Adv.*, 2023, **13**, 075301.
59 M. Mosavari, A. Khajehhaghverdi and R. M. Aghdam, *Inorg. Chem. Commun.*, 2023, 111293.
60 S. A. Thomas and J. Cherusseri, *Energy Storage*, 2023, e475.
61 W. Song, Q. Chen, K. Yang, M. Liang, X. Yi, J. Wang, J. Li and Z. Liu, *Adv. Funct. Mater.*, 2023, **33**, 2209880.
62 M. Chen, Y. He and J. Zhu, *Plasmonics*, 2019, **14**, 1019–1027.
63 E. R. Encina and E. A. Coronado, *J. Phys. Chem. C*, 2016, **120**, 5630–5639.
64 D. Li, Q. Zhang, L. Xing and B. Chen, *J. Laser Med. Sci.*, 2022, **37**, 3269–3277.
65 N. Hadilou, S. Souri, H. Navid, R. S. Bonabi, A. Anvari and B. Palpant, *Phys. Chem. Chem. Phys.*, 2020, **22**, 14318–14328.
66 C. Wang, H. Wang, L. Li, R. Zhao, J. Han and L. Wang, *Fuel*, 2024, **355**, 129537.
67 S. H. Lee and B.-H. Jun, *Int. J. Mol. Sci.*, 2019, **20**, 865.
68 H. Sies, V. V. Belousov, N. S. Chandel, M. J. Davies, D. P. Jones, G. E. Mann, M. P. Murphy, M. Yamamoto and c. Winterbourn, *Nat. Rev. Mol. Cell Biol.*, 2022, **23**, 499–515.
69 X. Meng, L. Liu, S. Ouyang, H. Xu, D. Wang, N. Zhao and J. Ye, *Adv. Mater.*, 2016, **28**, 6781–6803.
70 P. Bhatia, *Opt. Quantum Electron.*, 2023, **55**, 928.
71 A. G. Kumela, A. B. Gemta, T. A. Desta and A. Kebede, *RSC Adv.*, 2022, **12**, 16203–16214.
72 H. Tahara, M. Sakamoto, T. Teranishi and Y. Kanemitsu, *Nat. Commun.*, 2018, **9**, 3179.
73 M. Ivanchenko, A. L. Carroll, A. B. Brothers and H. Jing, *RSC Adv.*, 2023, **13**, 31569–31577.
74 X. Cui, Q. Ruan, X. Zhuo, X. Xia, J. Hu, R. Fu, Y. Li, J. Wang and H. Xu, *Chem. Rev.*, 2023, **123**, 6891–6952.
75 A. Ahmadivand and N. Pala, *Plasmonics*, 2016, **11**, 493–501.
76 M. Peng, H. Luo, W. Xiong, T. Kuang, X. Chen, X. Han, G. Xiao and Z. Tan, *Opt. Express*, 2022, **30**, 46060–46069.
77 D. P. Joshi and J. S. Aulakh, in *Ferrite Nanostructured Magnetic Materials*, Elsevier, 2023, pp. 197–222.
78 F. Ahmadpoor, S. A. Shojaosadati, H. Delavari, G. Christiansen and R. Saber, *Mater. Res. Express*, 2018, **5**, 055038.
79 G. Du, X. Zhou, C. Pang, K. Zhang, Y. Zhao, G. Lu, F. Liu, A. Wu, S. Akhmadaliev, S. Zhou, *et al.*, *Adv. Opt. Mater.*, 2020, **8**, 2000426.
80 B. K. Singh, V. Bambole, V. Rastogi and P. C. Pandey, *Opt Laser. Technol.*, 2020, **129**, 106293.
81 R. Wang, H. Xia, D. Zhang, J. Chen, L. Zhu, Y. Wang, E. Yang, T. Zang, X. Wen, G. Zou, *et al.*, *Nat. Commun.*, 2017, **8**, 14330.
82 E. Rafiee, *Plasmonics*, 2023, 1–7.
83 A. El Mouncharih, R. Takassa, O. Farkad, A. Tchenka, F. Elfatouaki, E. A. Ibnouelghazi and D. Abouelaoualim, *J. Nanophotonics*, 2023, **17**, 026007.
84 A. Bijalwan, B. K. Singh and V. Rastogi, *Optik*, 2021, **226**, 165994.
85 S. Sharma and A. Kumar, *Plasmonics*, 2022, **17**, 675–680.
86 D. Gowdhami and V. Balaji, *Opt. Quantum Electron.*, 2024, **56**, 593.
87 R. Jannesari, G. Pühringer, G. Stocker, T. Grille and B. Jakoby, *Sensors*, 2023, **24**, 193.
88 W. A. Müller, L. D. F. Marczak and J. R. Sarkis, *Trends Food Sci. Technol.*, 2020, **99**, 650–659.
89 L. Guillier, S. Martin-Latil, E. Chaix, A. Thébault, N. Pavio, S. Le Poder, C. Batéjat, F. Biot, L. Koch, D. W. Schaffner, *et al.*, *Appl. Environ. Microbiol.*, 2020, **86**, e01244.
90 G. Mendes-Oliveira, A. J. Deering, M. F. San Martin-Gonzalez and O. H. Campanella, *Food Microbiol.*, 2020, **87**, 103382.
91 H. Weldekidan, V. Strezov, J. He, R. Kumar, S. Asumadu-Sarkodie, I. N. Doyi, S. Jahan, T. Kan and G. Town, *Energy Fuels*, 2019, **33**, 6509–6514.
92 R. A. Cengel, *Introduction to Thermodynamics and Heat Transfer*, McGraw-Hill, 2008.
93 A. Sharma, D. Kumar, A. Kumar, N. Faisal, N. Kumar, S. Pandey, S. M. Hasnain, T. M. Al-Hazani, A. A. AlKahtane, S. Alkahtani, *et al.*, *Sustainability*, 2023, **15**, 9286.